

A Computational Approach for Hypersonic Aerodynamic Analysis using the Newtonian Flow Theory

David Smalley (851643@swansea.ac.uk)

Faculty of Science and Engineering
Swansea University

Abstract – The past few years have seen a revitalisation in spaceflight – with the introduction and improvement of reusability, increased accessibility, and decreased cost meaning the number of vehicles being developed capable of extremely high speed has dramatically increased. This paper outlines an approach to hypersonic aerodynamic analyses using the modified Newtonian flow theory and incorporates these changes into a 2-dimensional and 3-dimensional MATLAB program. Using a range of geometries, from simplistic 2D shapes like circles and ellipses, to more demanding 3D aerodynamic analyses, the program is rigorously tested. The results obtained are compared against existing data to confirm validity of the method and efficacy of the code.

In all comparisons considered, the modified Newtonian flow program computes valid solutions for a range of geometries (including extremely complex 3D geometries), verifying the efficacy of this method and the capability of the code to be able to cope with complex shapes whilst still computing reasonable results.

Keywords – aerodynamics, computational, hypersonic, MATLAB, modified Newtonian flow

I. INTRODUCTION

From the introduction of the early rockets (such as the V1 and V2 in the 1940s [1]), hypersonic flow theory has been a branch of fluid mechanics in active development [2]. The past few years have seen a revitalisation in spaceflight – with the introduction and improvement of reusability, increased accessibility, and decreased costs meaning the number of vehicles capable of extremely high speed has dramatically increased. The most generally recognised of these being SpaceX's reusable Falcon 9 rockets and 'Starship' programme but other vehicles include NASA's X-43A 'Hyper-X' waverider test vehicle, and the Lockheed Martin SR-72 (in development [3]). However, the complexities involved in designing such spacecraft and spaceplanes remain a significant obstacle: propulsion systems [4], aerothermodynamic heating [5], aerodynamics and commercial viability all pose important challenges. Notably, the aerodynamic design of such a vehicle during flight at hypersonic velocities (most commonly accepted to be at a Mach number, $M > 5$ [6]) is a vital factor in the effective design and development of these vehicles. This project developed a code, programmed in MATLAB, capable of generating aerodynamic analyses of arbitrary

geometries during hypersonic flow conditions by implementing and utilizing the modified Newtonian flow theory (as proposed by Lester Lee in 1955 [7]) and rarefied (low density, compressible [5]) gas dynamics [1].

In 1687, Sir Isaac Newton published *Principia Mathematica*, in which he presented several 'propositions' that laid the foundations for his theories on the laws of motion. The most relevant of these propositions to this paper are Propositions 32 through to 35 [2]. Newton's postulates for the behaviour of fluid flows proved very poor in low-speed fluid dynamics applications but has since come into favour with the advent of hypersonic flow applications, providing the most direct and simple approach [1] with adequate accuracy [2]. During the 1955 International Aeronautical Conference, Lester Lees proposed a modification to Newton's sine-squared law for pressure coefficient from *Principia Mathematica*, relating the pressure coefficient to Mach number [4]. This provided a considerably more accurate approach for hypersonic aerodynamic applications [1].

This research paper will firstly present a brief overview of the Newtonian flow theory, then discuss the modifications that can be made to account for Mach number dependence and specific heat ratio. Having incorporated these modifications into a MATLAB program, a comprehensive testing of the capability of the modified programs (both the 2-dimensional case and 3-dimensional case) will be presented, using a range of geometries – from simple 2D shapes like circles and airfoils, to more demanding 3D aerodynamic analyses. Following this, a validation of the results will be undertaken using experimental data, primarily Hoerner's *Fluid Dynamic Drag* [8]. Since hypersonic flow conditions are extremely challenging to replicate in a laboratory environment, the Newtonian flow model, and its implementation within a simple to use MATLAB program, will provide a useful tool in determining the aerodynamic properties of user requested (or generated) geometries at user specified conditions, building upon Newton's flow theory to extract a more accurate result at lower Mach numbers [5].

II. BACKGROUND THEORY

A. Newtonian flow theory

To conduct an analysis of the hypersonic flow regime and its interaction with a body, a mathematical model capable of predicting how such a flow behaves is required. In the case of this paper, the mathematical model chosen is Sir Isaac Newton's flow model from the late 17th Century [4].

In preceding the Navier-Stokes equations that fundamentally govern all fluid flows, Newton's flow model is capable of computing analyses for hypersonic flow regimes in relation to an inclined plane without the complex considerations of the Navier-Stokes equations [2] and the random motion of particles at the fluid's static pressure as modern science now recognises [1].

Newton's flow model assumes the fluid flow as a stream of linear particles which, upon contact with a solid body, lose entirely their momentum normal to the surface, but conserve momentum tangential to the surface [1] as seen in Figure 1.

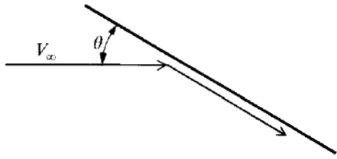


FIGURE 1
NEWTON'S FLOW MODEL SHOWING A STREAM WITH VELOCITY V_∞
IMPACTING A PLANE INCLINED AT AN ANGLE θ [1].

In the Newtonian flow theory, it is assumed no flow wraps around the edge of the plane and impacts the surface from behind. This phenomenon gives rise to a 'shadow' region behind the surface (Figure 2), in which there is no transfer of momentum to the rear of the surface. This allows for the assumption that $p = p_\infty$, thus resulting in a pressure coefficient, C_p , of zero [1], shown in Figure 2.

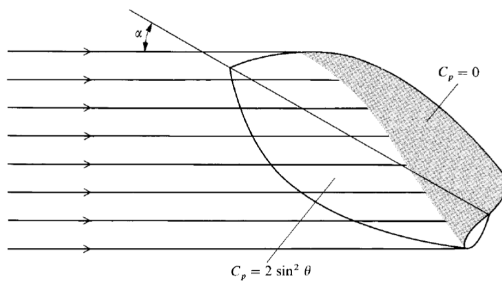


FIGURE 2
SHADOW REGION ACCORDING TO NEWTONIAN FLOW THEORY [1].

Considering the diagram in Figure 1, the component of the normal velocity, V_n , can be expressed as

$$V_n = V_\infty \sin \theta \quad (1)$$

and the volumetric flow rate within the control volume is given by

$$Q = VA = V_\infty A \sin \theta \quad (2)$$

where A is the frontal area of the surface.

Newton's second law of motion gives the normal force, F_n , as

$$F_n = \frac{d(mv)}{d(t)} = V_n \rho Q = V_\infty^2 \rho_\infty A \sin^2 \theta \quad (3)$$

or

$$\frac{F_n}{A} = V_\infty^2 \rho_\infty \sin^2 \theta \quad (3.1)$$

$\frac{F_n}{A}$ in (3.1) should be interpreted as the pressure difference above the freestream static pressure [1]

$$\frac{F_n}{A} = p - p_\infty \quad (4)$$

where p is the surface pressure and p_∞ is the freestream static pressure.

Equating (3.1) and (4) and algebraically manipulating leads to

$$C_p = \frac{p - p_\infty}{\frac{1}{2} \rho_\infty V_\infty^2} = 2 \sin^2 \theta \quad (5)$$

where C_p is the pressure coefficient and $\frac{1}{2} \rho_\infty V_\infty^2 = q_\infty$ is the far-field dynamic pressure. Equation 5 is Newton's famous sine-squared law for pressure coefficient.

From (5), the drag and lift coefficients can be expressed as

$$C_d = \frac{D}{q_\infty A} = \frac{F_n \sin \theta}{q_\infty A} = C_p \sin \theta = 2 \sin^3 \theta \quad (6)$$

$$C_l = \frac{L}{q_\infty A} = \frac{F_n \cos \theta}{q_\infty A} = C_p \cos \theta = 2 \sin^2 \theta \cos \theta \quad (7)$$

B. Accounting for Mach number

In *Hypersonic and High-Temperature Gas Dynamics*, Anderson states that "certain aerodynamic quantities become relatively independent of freestream Mach number, M_∞ , if M_∞ is sufficiently high" [1]. The pressure coefficient offered by the un-modified Newtonian flow theory epitomises this: as M_∞ tends towards infinity, un-modified Newtonian flow theory increases in accuracy [1] [7] (Figure 3). To improve the accuracy of the Newtonian flow method at low M_∞ , C_p can be related to M_∞ by the inclusion of stagnation pressure coefficient, $C_{p,max}$ [7]. Therefore, the modified pressure coefficient is

$$C_p = C_{p,max} \sin^2 \theta \quad (8)$$

$C_{p,max}$ is defined as

$$C_{p,max} = \frac{p_{02} - p_\infty}{\frac{1}{2} \rho_\infty V_\infty^2} \quad (9)$$

where p_{02} is the pressure at the stagnation point behind the normal shock (the local surface inclination is 90° , resulting in $\sin \theta = 1$, thus $p = p_{02}$), and the Rankine-Hugoniot relation gives (10), equivalent to Rayleigh's supersonic pitot tube formula.

$$\frac{p_{02}}{p_\infty} = \left[\frac{(\gamma + 1)^2 M_\infty^2}{4\gamma M_\infty^2 - 2(\gamma - 1)} \right]^{\frac{\gamma}{\gamma-1}} \left[\frac{1 - \gamma + 2\gamma M_\infty^2}{\gamma + 1} \right] \quad (10)$$

Noting that $\frac{1}{2} \rho_\infty V_\infty^2 = \frac{\gamma}{\gamma+1} p_\infty M_\infty^2$, (9) can be re-written as

$$C_{p,max} = \frac{2}{\gamma M_\infty^2} \left[\frac{p_{02}}{p_\infty} - 1 \right] \quad (11)$$

By combining (10) and (11),

$$C_{p,max} = \frac{2}{\gamma M_\infty^2} \left\{ \left[\frac{(\gamma + 1)^2 M_\infty^2}{4\gamma M_\infty^2 - 2(\gamma - 1)} \right]^{\frac{\gamma}{\gamma-1}} \cdots \left[\frac{1 - \gamma + 2\gamma M_\infty^2}{\gamma + 1} \right] - 1 \right\} \quad (12)$$

Therefore, the pressure coefficient in the modified Newtonian flow method is the combination of (8) and (12)

$$C_p = \frac{2}{\gamma M_\infty^2} \left\{ \left[\frac{(\gamma + 1)^2 M_\infty^2}{4\gamma M_\infty^2 - 2(\gamma - 1)} \right]^{\frac{\gamma}{\gamma-1}} \cdots \left[\frac{1 - \gamma + 2\gamma M_\infty^2}{\gamma + 1} \right] - 1 \right\} \sin^2 \theta \quad (13)$$

Drag and lift coefficients can be found by substituting (13) into (6) and (7), respectively.

This modified pressure coefficient forces the modified Newtonian flow theory to be exact at the stagnation point [1], greatly increasing the accuracy, as demonstrated in Figure 4. For blunt-nosed bodies, this modification to the Newtonian flow theory proves especially accurate [1].

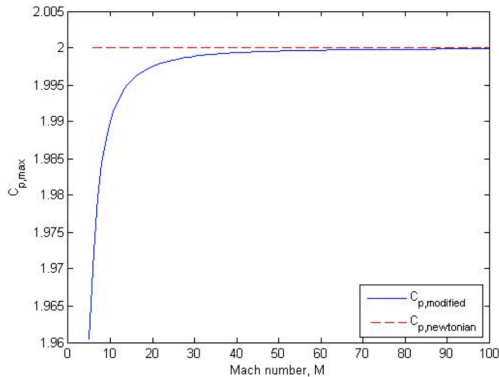


FIGURE 3

PLOT OF THE $C_{p,max}$ FROM THE MODIFIED AND UNMODIFIED NEWTONIAN THEORY AGAINST MACH NUMBER. THIS SHOWS UNITY AS $M_\infty \rightarrow \infty$ AND $\gamma \rightarrow 1$, YIELDING $C_p \rightarrow 2 \sin^2 \theta$.

To modify both codes, (13) was implemented in each of the codes as well as requesting an input M and γ to fulfil the computation using the modified Newtonian method.

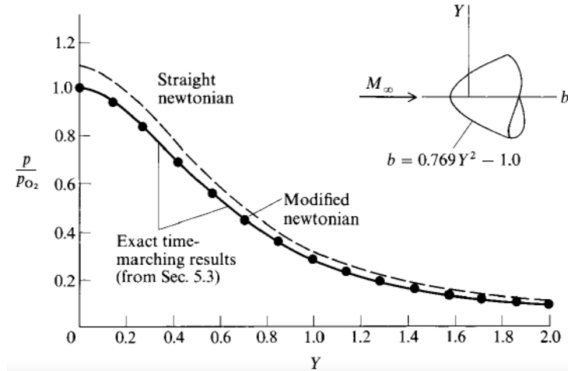


FIGURE 4

COMPARISON OF UNMODIFIED AND MODIFIED NEWTONIAN FLOW THEORIES, AND EMPIRICAL DATA FOR A BLUNT BODY AT MACH 8 [1]. THIS SHOWS THE MODIFIED NEWTONIAN METHOD IMPROVES SIGNIFICANTLY UPON THE STRAIGHT NEWTONIAN MODEL.

C. Base Code Overview

a. 2D Application

For a detailed explanation of the code into which the modifications (listed in Section III, Sub-Heading D) were implemented, the reader is directed to Morgan and Bagwell's thesis [10]. To summarise, the computer program sections a user requested geometry into panels upon which a computation of C_p using (5) is undertaken. To provide accurate results, a panel refinement scheme is used. This increases the number of panels whilst simultaneously reducing the size of each panel until the desired accuracy is reached [10].

To conserve computing resources, a selective refinement algorithm is required. Since $C_p = 0$ in the shadow region, an accurate geometry, mesh and pressure coefficient calculation is not required here. Figure 5 displays a selectively re-panelled 2D shape.

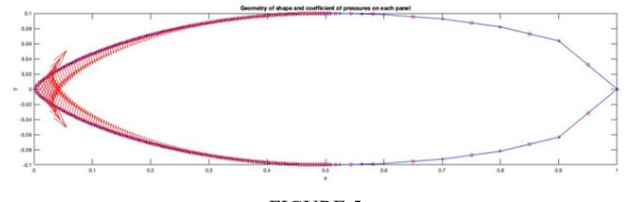


FIGURE 5

2D SEARS-HAACK BODY. NOTE THE PANELLING RESOLUTION DECREASES SIGNIFICANTLY BEHIND THE POINT OF MAXIMUM THICKNESS.

b. 3D Application

The Delaunay triangulation method is used to create 3D panels (elements) on the surface of the shape [11] and define the geometry. Each surface is analysed using vector algebra [1], allowing for the calculation of each element's pressure coefficient using (5), as shown in Figure 6. An example of this methodology in use can be seen in Figure 7.

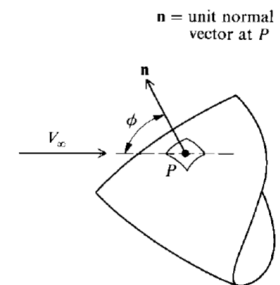


FIGURE 6
GEOMETRY FOR THE 3D APPLICATION OF NEWTONIAN FLOW THEORY [1].

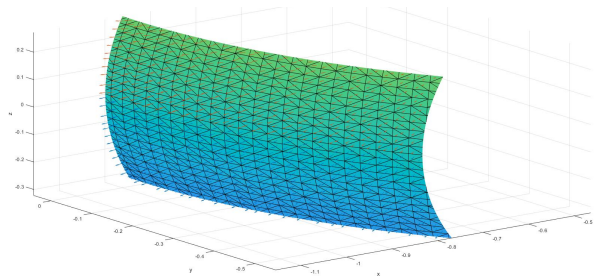


FIGURE 7
DELAUNAY MESH ON MAGNIFIED AREA OF A SPHERE.

III. METHOD

D. Implementation of the modified Newtonian flow theory into the MATLAB program

To account for Mach number dependence, the standard Newtonian flow codes outlined in Sub-Section C is revised by the replacement of the sine-squared law (5.2) with Lees modified expression for pressure coefficient (12, 13). To achieve this, both 2D and 3D codes include two necessary additions to the initial user prompts: Mach number, M , and specific heat ratio, γ , for $C_{p,max}$ to be calculated. The modified C_p is then computed using (13). Following this, C_d and C_l are found as per (6) and (7) respectively. The proceeding code remains unmodified to preserve the geometry and meshing algorithms constructed in [10].

In addition to the implementation of the modified Newtonian flow method, other refinements and adjustments are made to both codes. Namely, this includes a reduction in error tolerance in the 2D code to guarantee convergence, increasing the accuracy of results on complex geometries whilst maintaining a reasonable computation time. Furthermore, if instructed to carry out the analysis over a range of angle of attacks, α , the 2-dimensional code automatically saves α , C_l , C_d and lift-to-drag ratio to a Microsoft Excel file; this allows for more easily accessible numerical data for further analysis.

The 3D code is modified to include a timer to better help evaluate the run time and thus the program's performance.

E. Geometry creation and input format

To broaden the applications of this Newtonian flow solver, both 2D and 3D codes contain the option for user defined input geometries.

a. 2-Dimensional Approach

If the user defined shape input is chosen in 2D program, the code reads a set of coordinate points, listed in a Microsoft Excel ‘.xlsx’ file which the user defines, as shown in Figure 8. By reading only columns A through D, additional shape variables and shape plots can be utilised to define and visually confirm the coordinates' geometry.

For simple geometries with sharp vertices on a continuous line, it is recommended to concentrate coordinates either side of the vertex to minimise the variation introduced by the spline function within MATLAB. This can be seen in Figure 9.

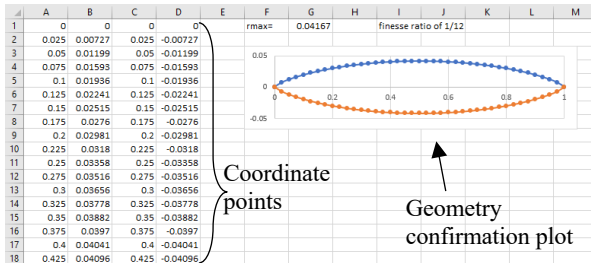
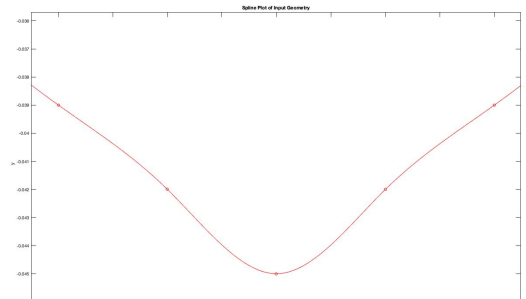
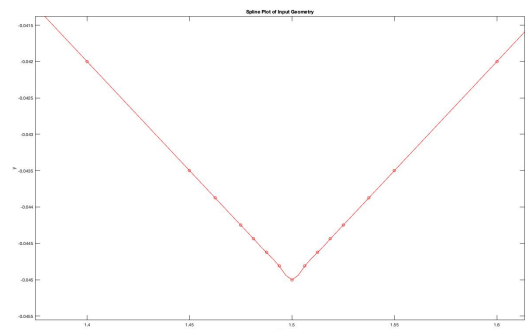


FIGURE 8
EXAMPLE OF USER DEFINED COORDINATE POINTS OF A SEARS-HAACK [12] BODY WITH A FINESSE RATIO (LENGTH TO WIDTH) OF 1/6.



(a)



(b)

FIGURE 9
LINEARLY SPACED COORDINATE POINTS (a) AND REFINED COORDINATE POINTS AROUND A VERTEX (b), MAGNIFIED.

b. 3-Dimensional Approach

The 3D code employs a similar approach to the 2D code: the user firstly selects a user defined shape, in the form of a STL file. These are obtained either by purchase from Computer Aided Design (CAD) exchange websites or constructed in CAD software such as SolidWorks. Figure 10 shows a scale SolidWorks model of NASA's X-43A 'Hyper-X' test waverider vehicle [13] that is subsequently meshed and analysed using the modified Newtonian flow program.

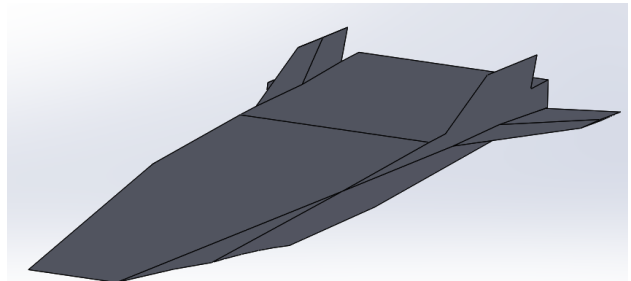


FIGURE 10
CAD MODEL OF NASA'S X-43A [13], SCRAMJET OMITTED.

IV. RESULTS

F. 2-Dimensional Results

The following results were all run at $M = 5$, $\gamma = 1.4$ (assuming air to be a perfect gas) and at $\alpha = 0^\circ$, unless otherwise stated. These results also include a plot of a sweep of angle of attacks of $0^\circ \leq \alpha \leq 20^\circ$, showing how C_L , C_D and lift-to-drag ratio vary with angle of attack. The computed values of C_L and C_D were found when the convergence error reached $1E - 05$.

Figures 11 to 13 show the results from a circle. Figures 14 to 16 show the results from an asymmetric airfoil, a NACA 2412. Following this are the results from the side profile of the Lockheed SR71B ‘Blackbird’ (Figures 17 to 19), a more complex 2D example.

Figure 11 demonstrates the ‘shadow’ region past the highest point of the geometry. The resultant lack of momentum transfer is reflected in the C_p , C_D and C_L values dropping to zero at this interface (Figure 12). This phenomenon can be seen similarly in the equivalent plots for the following geometries.

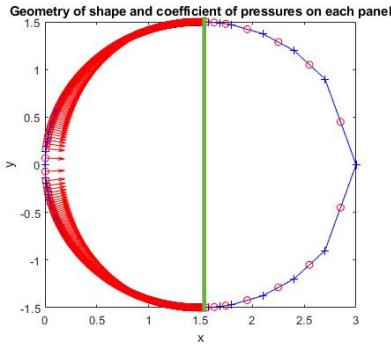


FIGURE 11

PRESSURE COEFFICIENT MAGNITUDE OF EACH PANEL (RIGHT). THE COMPUTED $C_L = 0$ AND $C_D = 1.21$. A GREEN VERTICAL LINE IS INCLUDED TO SHOW THE START OF THE SHADOW REGION (AT $x = 1.5$) IN THIS CASE, AS X INCREASES ALONG THE LENGTH OF THE SHAPE.

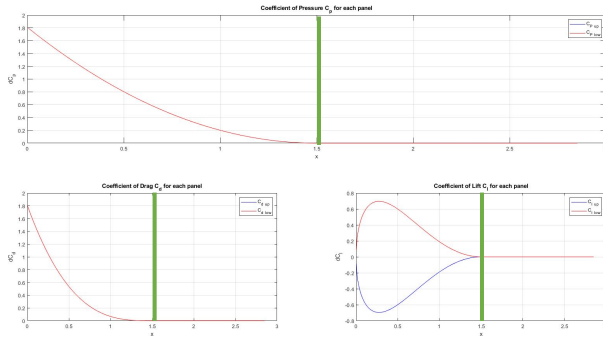


FIGURE 12

C_p (UPPER), C_D (LOWER, LEFT) AND C_L (LOWER, RIGHT), VARIATION ALONG THE CHORD, x . NOTE THE UPPER AND LOWER SURFACE RESULTS ARE DENOTED BY BLUE AND RED LINES, RESPECTIVELY. IN BOTH THE C_p AND C_D PLOTS, BOTH THE UPPER AND LOWER SURFACES’ RESULTS ARE EQUAL DUE TO THE INPUT GEOMETRY BEING SYMMETRICAL, RESULTING IN OVERLAPPING LINES. AS IN FIGURE 11, GREEN LINES DENOTE THE START OF THE SHADOW REGION AND DEMONSTRATE THE POINT AT WHICH EACH COEFFICIENT DROPS TO ZERO.

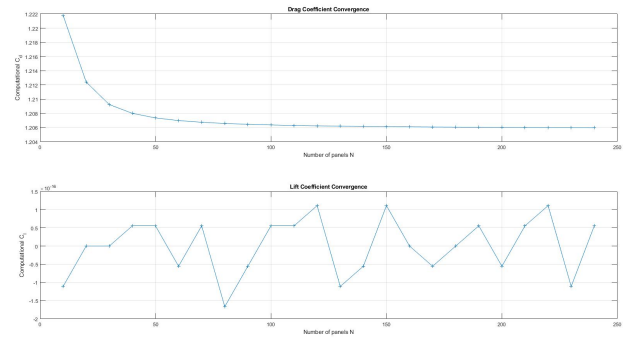


FIGURE 13

C_D CONVERGENCE (UPPER) AND C_L CONVERGENCE (LOWER) FOR A CIRCLE. WHILST THE C_L CONVERGENCE APPEARS UNSTABLE, NOTE THE Y-AXIS IS TO THE ORDER 10^{-16} : ANY DEVIATIONS ARE NEGLIGIBLE FROM THE TRUE CONVERGENCE VALUE OF ZERO.

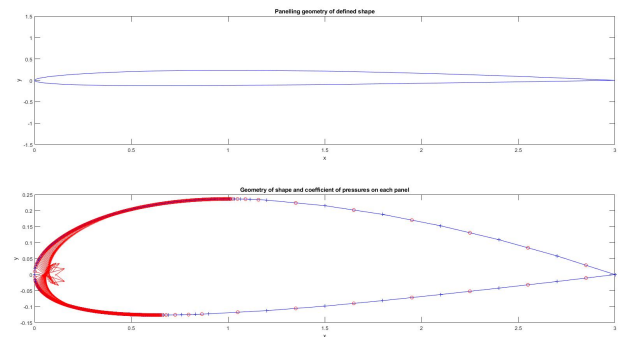


FIGURE 14

NACA 2412 GEOMETRY (UPPER) AND PRESSURE COEFFICIENT OF EACH PANEL (LOWER). THE COMPUTED $C_L = -0.0207$ AND $C_D = 0.0633$.

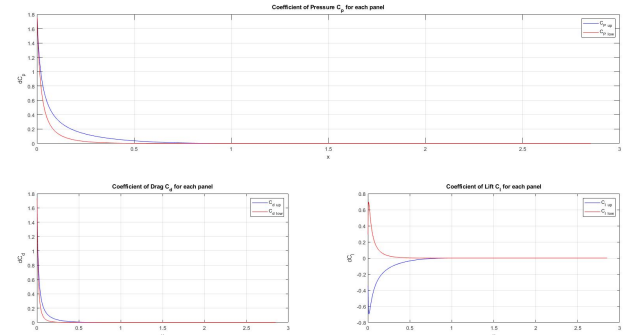


FIGURE 15

C_p (UPPER), C_D (LOWER LEFT) AND C_L (LOWER RIGHT), VARIATION ALONG THE CHORD, x .

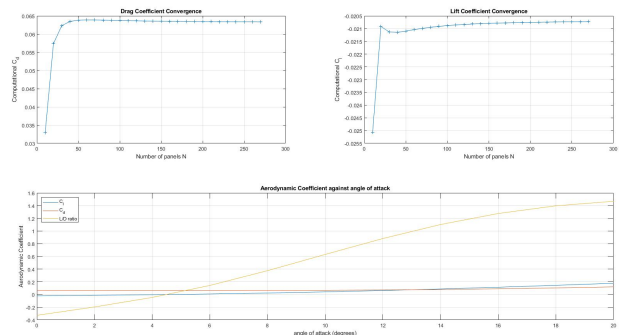


FIGURE 16

C_D CONVERGENCE (UPPER LEFT) AND C_L CONVERGENCE (UPPER RIGHT) FOR A NACA 2412 AIRFOIL, AND ∞ SWEEP (LOWER).

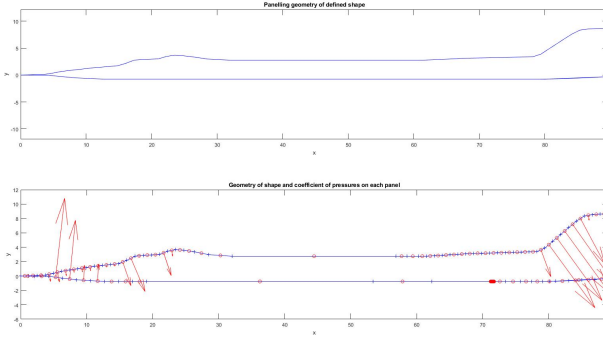


FIGURE 17

SR71B SIDE PROFILE (UPPER) AND PRESSURE COEFFICIENT OF EACH PANEL (LOWER). THE COMPUTED $C_L = -0.0631$ AND $C_D = 0.0397$.

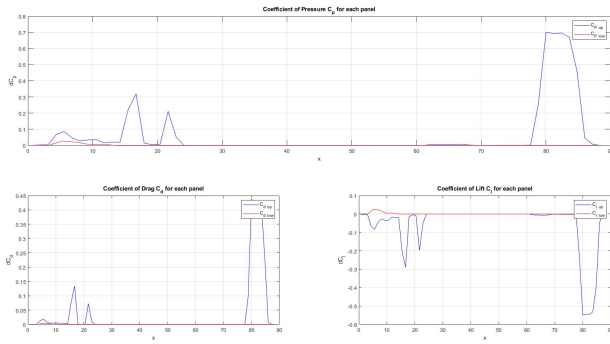


FIGURE 18

C_p (UPPER), C_D (LOWER LEFT) AND C_L (LOWER RIGHT), VARIATION ALONG THE CHORD, x .

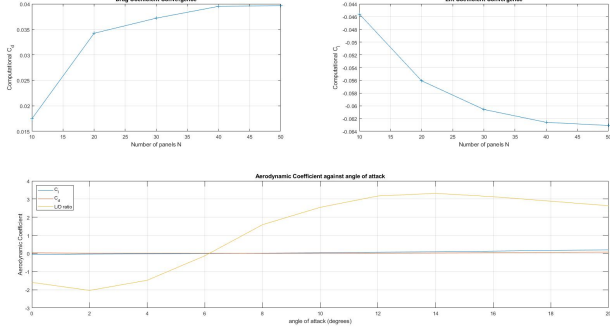


FIGURE 19

C_D CONVERGENCE (UPPER LEFT) AND C_L CONVERGENCE (UPPER RIGHT) FOR A SR71B, AND α SWEEP (LOWER).

Figures 17 and 18 demonstrate the main contributors to surface pressure on the SR71B at moderately high Mach number ($M = 5$): the leading edges of the nose, cockpit, and the vertical tail.

G. 3-Dimensional Results

Similarly to the 2D results, all the following tests were run at $M = 5$, $\gamma = 1.4$ (assuming air to be a perfect gas) and at an angle of attack, $\alpha = 0^\circ$, unless otherwise stated. The computed values of C_L and C_D were found when the convergence error reached $1E - 06$.

Starting with a simple 3D shape, figures 20 to 22 show the results for a sphere.

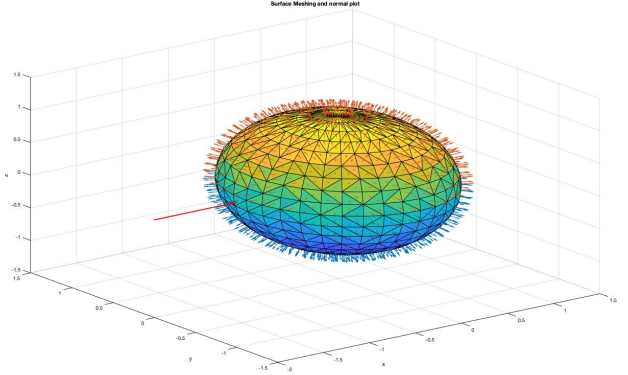


FIGURE 20

SURFACE MESH OF SPHERE. THE RED ARROW SHOWS THE DIRECTION OF THE FREESTREAM. THE COMPUTED $C_L = 0$ AND $C_D = 0.904$.

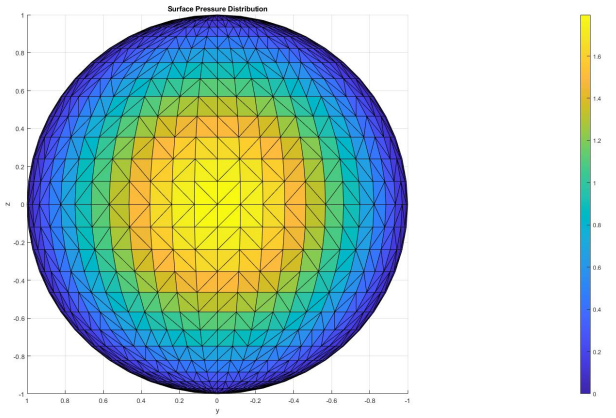


FIGURE 21

SURFACE DISTRIBUTION OF COEFFICIENT OF PRESSURE OF SPHERE.

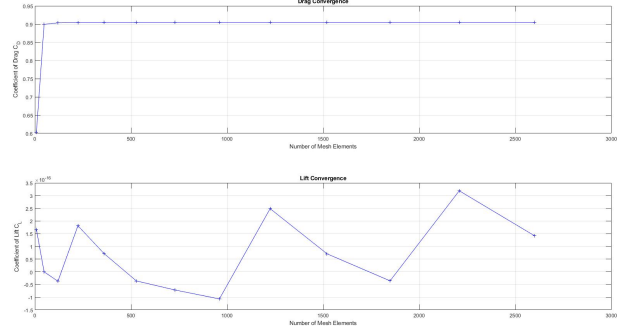


FIGURE 22

DRAG (UPPER) AND LIFT (LOWER) CONVERGENCE AGAINST NUMBER OF MESH ELEMENTS PLOTS. AS SEEN IN FIGURE 13, THE LIFT COEFFICIENT CONVERGENCE APPEARS UNSTABLE. HOWEVER, IT IS IMPORTANT TO NOTE THE CONVERGENCE SCALE, 10^{-16} . THEREFORE, IT IS REASONABLE TO ASSUME THE COMPUTATION HAS REACHED CONVERGENCE.

Figures 23 and 24 show the outputs for an asymmetric airfoil (NACA 2412), with no taper. The computed lift coefficient was -0.0187 and computed drag coefficient was 0.0627 . Figure 25 demonstrates a 3-dimensional case of the shadow region, noting the gradient to dark blue (indicating a region of $C_p = 0$) soon after the leading edge.

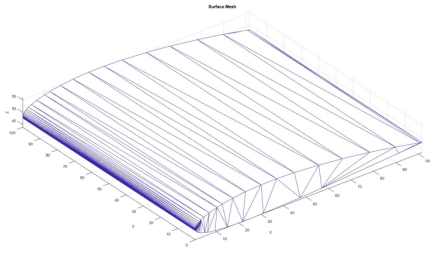


FIGURE 23
SURFACE MESH OF A NACA 2412, ASYMMETRIC AIRFOIL.

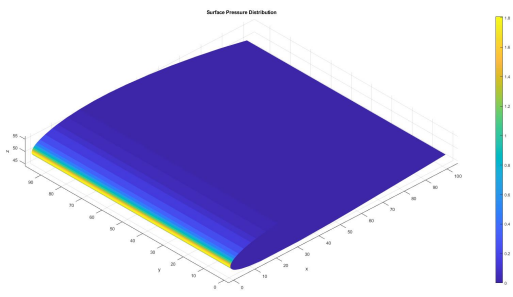


FIGURE 24
PRESSURE COEFFICIENT SURFACE DISTRIBUTION OF A NON-TAPERED NACA 2412 (ASYMMETRIC) AIRFOIL.

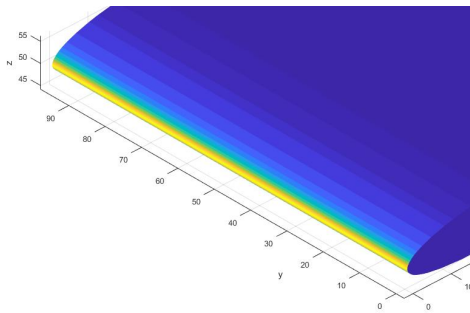


FIGURE 25
LEADING EDGE OF THE NACA 2412 SEEN IN FIGURE 24, SHOWING THE TRANSITION TO THE SHADOW REGION (YELLOW TO DEEP BLUE).

Figures 26 and 27 show results for a Space Shuttle at Mach 5. This model is an idealised approximation due to the lack of surface details and imperfections but serves as a useful visual aid. The computed lift and drag coefficients for this model under these conditions were $C_L = 0.0267$ and $C_D = 0.0411$. Figures 28 to 30 show the same model in conditions more representative of the real-world vehicle at the start of its re-entry: Mach 25 and an angle of attack of 40° . For these conditions, $C_L = -0.368$ and $C_D = 0.345$.

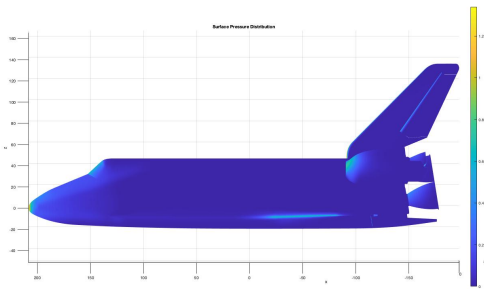


FIGURE 26
SURFACE DISTRIBUTION OF PRESSURE COEFFICIENT OF AN APPROXIMATE GEOMETRY OF A NASA ORBITER (SPACE SHUTTLE), SIDE PROFILE VIEW.

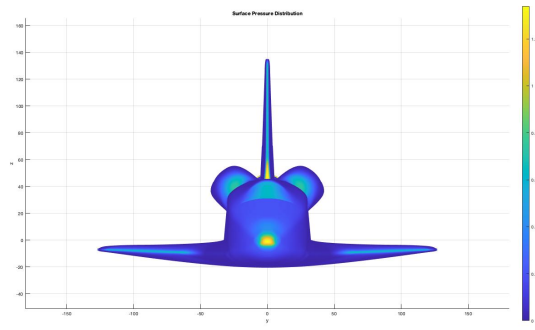


FIGURE 27
SURFACE DISTRIBUTION OF PRESSURE COEFFICIENT OF AN APPROXIMATE GEOMETRY OF A NASA ORBITER (SPACE SHUTTLE), FRONT VIEW.

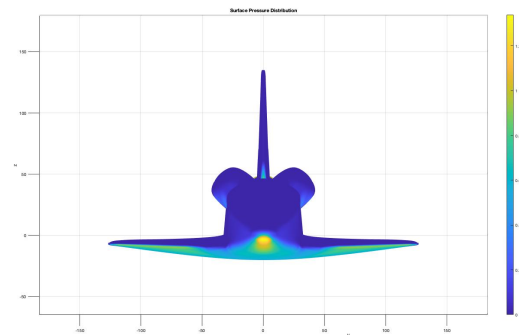


FIGURE 28
SURFACE DISTRIBUTION OF PRESSURE COEFFICIENT OF AN APPROXIMATE GEOMETRY OF A NASA ORBITER (SPACE SHUTTLE) DURING INITIAL RE-ENTRY CONDITIONS, FRONT VIEW.

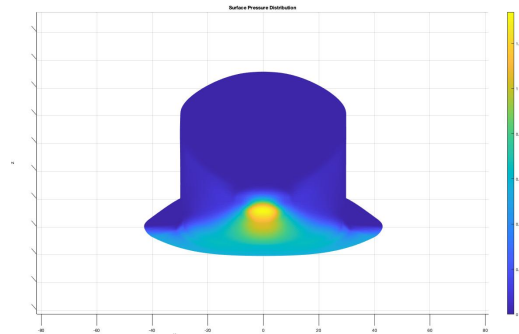


FIGURE 29
ZOOMED IN TO THE NOSE OF THE SHUTTLE SEEN IN FIGURE 28.

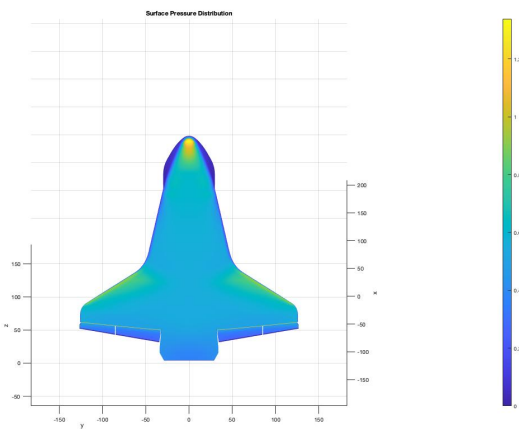
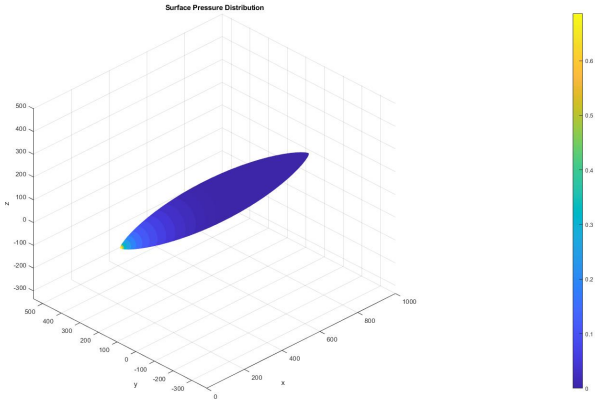
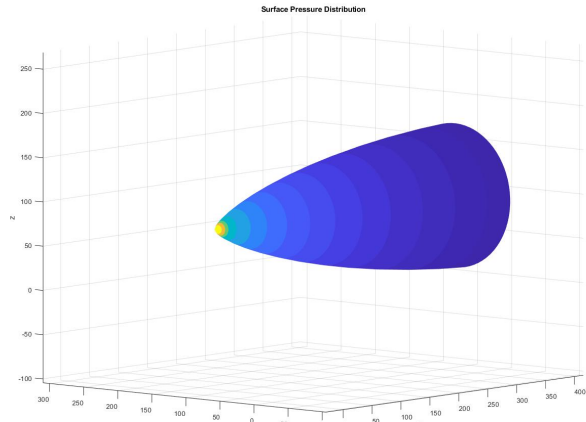


FIGURE 30
UNDERSIDE OF THE SHUTTLE DURING INITIAL RE-ENTRY CONDITIONS.



(a): DISTRIBUTION OF PRESSURE COEFFICIENT FOR SEARS-HAACK BODY



(b): SEARS-HAACK NOSE, MAGNIFIED

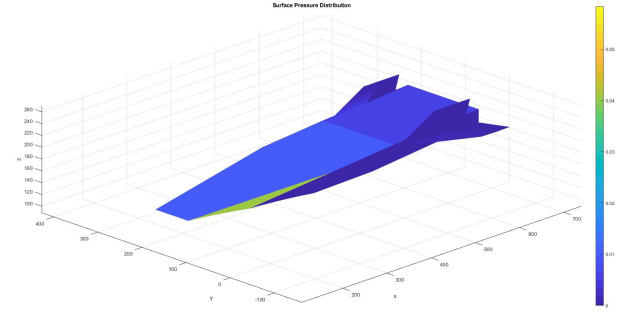
FIGURE 31

SURFACE DISTRIBUTION OF PRESSURE COEFFICIENT FOR SEARS-HAACK BODY WITH FINESSE RATIO OF 1/6.

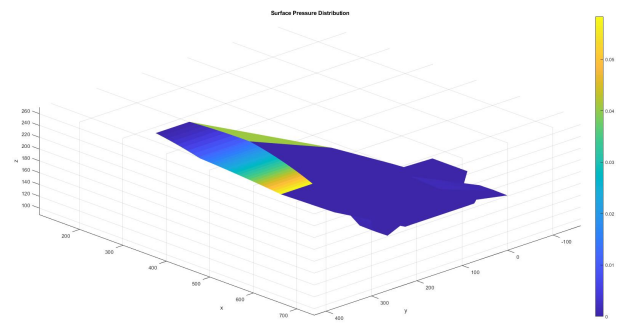
The computed drag coefficient of the above Sears-Haack body was 0.0139, and the computed lift coefficient was 0. This C_L value was to be expected due to the body's symmetrical reference area. As expected with a Sears-Haack body, Figure 31b shows a gradual distribution of surface pressure.

Figure 32 shows the NASA X-43A waverider testbed detailed in figures 10 and 11. The results for this aircraft were computed from its world-record beating flight at Mach 9.6 [13]. The scramjet was omitted, and the airframe geometry simplified and approximated with the use of scale, 3-view drawings, offering an inexact, but satisfactory, indication of the X-43A's aerodynamic performance at its top speed.

The curved underside surface seen in Figure 32b can be seen to be the primary source of pressure for this vehicle. This was expected due to the nature the X-43A generates lift: compression lift [1], hence the 'waverider' label.



(a): UPPER SIDE ISOMETRIC VIEW



(b): UNDERSIDE ISOMETRIC VIEW

FIGURE 32
SURFACE DISTRIBUTION OF PRESSURE COEFFICIENT FOR X-43A AT MACH 9.6.

For these flight conditions, the modified Newtonian theory program computed a C_L and C_D of -0.00213 and 0.0015 respectively, at $\alpha = 0^\circ$.

To comprehensively test the modified Newtonian flow code, an extremely complex geometry of a Formula 1 car was tested. Although not directly applicable to the flow conditions the Formula 1 racecar would experience, the complexity of the body was able to verify the efficacy of the code, even when presented with unrealistic bodies.

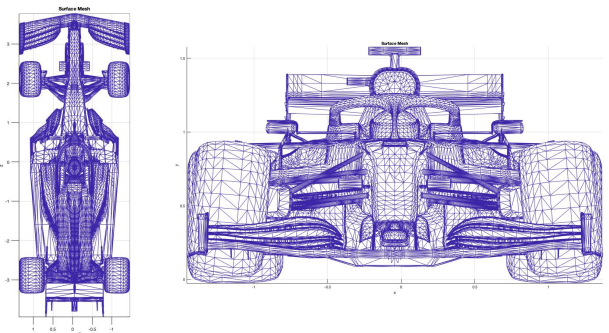


FIGURE 33
TOP (LEFT) AND FRONT (RIGHT) VIEWS OF THE MESH GENERATED FOR THE TEST FORMULA 1 CAR (A RED BULL RACING RB16B) [14].

The RB16b Formula 1 car was tested at $M = 5$ and yielded a $C_L = 0.000017$ and $C_D = 0.848$, at $\alpha = 0^\circ$. Although these values offer little usefulness in direct relation to the design of the Formula 1 car, Figure 34 demonstrates the principal contributors to surface pressure: the front and rear tyres and the front and rear wings. This correlates to Taylors' results for a comparable Formula 1 car [15].

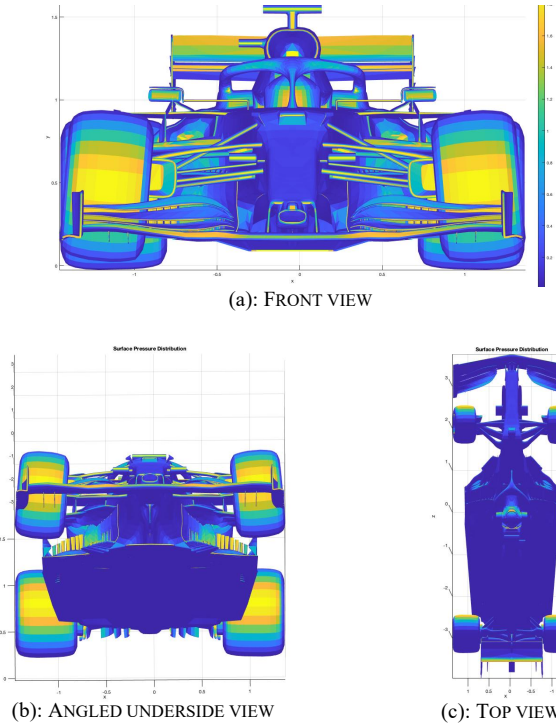


FIGURE 34

SURFACE DISTRIBUTION OF PRESSURE COEFFICIENT FOR RB16B F1 CAR. SUB-FIGURE (b) DETAILS SHAPES HIDDEN BY FRONT WING ASSEMBLY, FOR EXAMPLE, BARGEBOARDS. SUB-FIGURE (c) DEMONSTRATES CLEAR SHADOW REGIONS (DEEP BLUE) THAT PARTLY CONTRIBUTE TO MAINTAINING A REASONABLE COMPUTATION RUN TIME.

H. Validation of Results using Empirical Data

Here, the validity of the modified Newtonian method, and its implementation into a computational approach, is compared against the empirical data and plots found in Hoerner's *Fluid Dynamic Drag* [8]. For this, comparable geometries to those found in [8] were constructed in SolidWorks and subsequently tested under the same conditions specified in [8].

Firstly, the drag coefficient at $M = 6$ (and $\gamma = 1.4$) of varied nosecone leading edge geometry was evaluated. Figures 35 and 36 show examples of a wedge and circular leading edge respectively, both with an x (length of leading edge) to t (maximum diameter) ratio of 2:1. Similar geometries were constructed with a range of x/t ratios and tested at the same conditions.

The plot shown in Figure 37 demonstrates a close correlation of the modified Newtonian theory and real-world, empirical data.

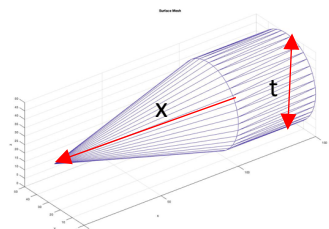


FIGURE 35

MESHED EXAMPLE OF A 2:1 BLUNT WEDGE LEADING EDGE.

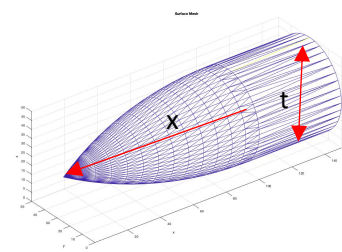


FIGURE 36

MESHED EXAMPLE OF A 2:1 BLUNT CIRCULAR LEADING EDGE.

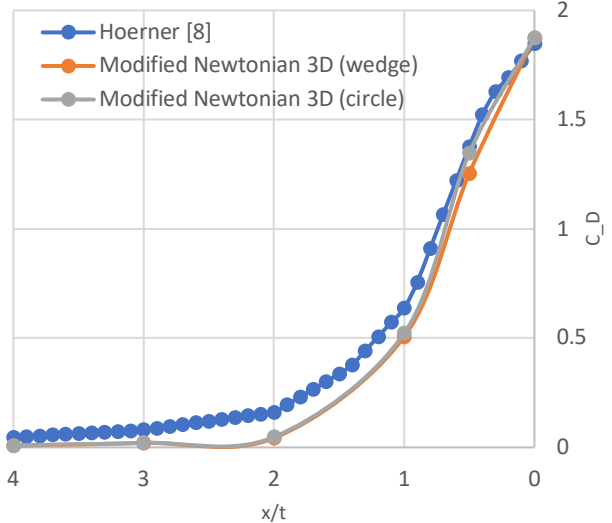


FIGURE 37

COMPARISON OF C_D AND METHODOLOGY AT HYPERSONIC SPEEDS DUE TO BLUNT LEADING EDGES AS A FUNCTION OF THEIR SHAPE. HOERNER'S EMPIRICAL DATA [8] IS PLOTTED IN BLUE, THE ORANGE AND GREY LINES SHOW THE MODIFIED NEWTONIAN FLOW METHOD RESULTS OF WEDGE AND CIRCULAR LEADING EDGES, RESPECTIVELY.

To further illustrate the effectiveness of the modified Newtonian flow method and its implementation within the code, a second comparison with a different set of data was conducted. Here, the effect of fillet radius of a blunt body on drag coefficient was tested and compared to data found in [8]. Figure 38 shows how the r/d (fillet radius to total diameter) ratio is defined [8].



FIGURE 38

GEOMETRIC DEFINITION OF FILLET RADIUS, r , AND DIAMETER, d [8].

Using these definitions, a range of blunt bodies were made in SolidWorks with varying r/d ratios, to gather a set of 3D geometries to be compared with Hoerner's empirical data. Figure 39 shows the result of this comparison at 2 different Mach numbers as defined by Hoerner [8].

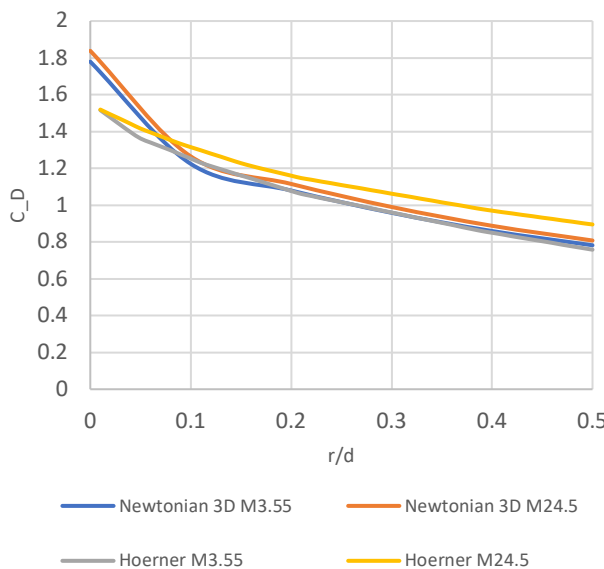


FIGURE 39

DRAG AT HYPERSONIC SPEEDS DUE TO ROUNDED LEADING EDGES AS A FUNCTION OF THEIR DIAMETER TO LEADING EDGE RADIUS. A CLOSE EQUIVALENCE CAN BE OBSERVED BETWEEN THE MODIFIED NEWTONIAN METHOD AND EMPIRICAL DATA.

V. CONCLUSION

This paper has outlined the mathematical models of both un-modified and modified Newtonian flow methods and presented a computational approach to hypersonic aerodynamic analysis using the modified Newtonian flow theory. The modified codes were tested extensively using a variety of shapes, including bodies outside of the scope traditionally tested in hypersonic aerodynamic solvers. In all cases, the codes ran acceptably quickly (the 2D code computed results in less than 1 minute for all geometries (α sweep notwithstanding); the 3D code computed results in the scope of less than 1 minute to 10 minutes (depending on mesh element number), using 2017 Apple MacBook Air with an Intel i5 Dual-Core processor (1.8GHz).

Selected geometries were run and compared to empirical data. In all comparisons, the modified Newtonian theory codes presented valid solutions that closely matched empirical data. This demonstrated the effectiveness of both codes as well as the modified Newtonian flow theory in hypersonic aerodynamic applications.

To further improve the program, a representation of the flow-field around the body could be implemented however, due to the nature of the Newtonian flow model, this would not impact the solutions significantly. Therefore, the modified Newtonian flow method is a valid method for rapid evaluation of a body's aerodynamic characteristics in hypersonic flow conditions. An additional feature that could be included is a wall temperature solver. This would provide a useful tool in the preliminary design of hypersonic vehicles, given the design precedent temperature takes. Coupled with an evolutionary optimisation algorithm, bodies could be optimised for surface temperature distribution at key Mach numbers,

similar to Evans and Walton's re-entry vehicle optimisation using the Boltzmann-BGK equation [16].

It is interesting to note the various extensions of the Newtonian model and their applications, details of which can be found in [1] [2] [7] [17].

VI. ACKNOWLEDGEMENT

I would like to express my gratitude to Dr Ben Evans for his guidance, supervision, and support throughout the duration of this project.

VII. REFERENCES

- [1] Anderson J. Hypersonic and High-Temperature Gas Dynamics. 2nd ed. American Institute of Aeronautics and Astronautics; 2006.
- [2] Hayes W, Probstein R. Hypersonic Flow Theory. New York: Academic Press; 1966. p. 70-75
- [3] SR-72 Hypersonic Demonstrator Aircraft [Internet]. Airforce Technology. 2022 [cited 8 March 2022]. Available from: <https://www.airforce-technology.com/projects/sr-72-hypersonic-demonstrator-aircraft/>
- [4] Küchmann D. The Aerodynamic Design of Aircraft. Virginia: American Institute of Aeronautics and Astronautics; 2012.
- [5] Panaras A. Aerodynamic Principles of Flight Vehicles. Reston, VA: American Institute of Aeronautics and Astronautics; 2012.
- [6] Anderson J. Fundamentals of Aerodynamics. 6th ed. New York: McGraw-Hill Education; 2017.
- [7] Lees L. Hypersonic Flow. Fifth International Aeronautical Conference. 1955; p. 241-276.
- [8] Hoerner S. (ed.) Fluid-Dynamic Drag. 1965. p. 384-409, 437-445
- [9] Mason W. Hypersonic Aerodynamics [Internet]. Virginia Tech, Department of Aerospace and Ocean Engineering. 2017 [cited 9 March 2022]. Available from: http://www.dept.aoe.vt.edu/~mason/Mason_f/ConfigAeroHypersonic.pdf
- [10] Bagwell S, Morgan K. A Hypersonic Flow Model for the Aid of Conceptual Design of Re-Entry Vehicles [Undergraduate]. Swansea University
- [11] Cheng S, Dey T, Shewchuk J, Sahni S. Delaunay Mesh Generation: Algorithms and Mathematical Analysis. Taylor & Francis Group; 2013.
- [12] Sears, W., 1947. On Projectiles of Minimum Wave Drag. *Quarterly of Applied Mathematics*, [online] 4(4), pp.361-366. Available at: <https://www.ams.org/journals/qam/1947-04-04/S0033-569X-1947-20394-7/S0033-569X-1947-20394-7.pdf> [Accessed 10 March 2022].
- [13] Conner, M., 2017. X-43A (Hyper-X). [online] NASA. Available at: https://www.nasa.gov/centers/armstrong/history/experimental_aircraft/X-43A.html [Accessed 11 March 2022].
- [14] Sketchfab. 2022. Sketchfab. [online] Available at: <https://sketchfab.com/3d-models/red-bull-rb16b-free-c6db515741394d2daf0d29f88721ff34> [Accessed 23 February 2022; page deleted on 20 April 2022].
- [15] 2021 Williams F1 CFD [Internet]. Max Taylor. 2021 [cited 1 May 2022]. Available from: <https://maxtaylor.aero.wordpress.com/2021/04/21/2021-williams-f1-cfd/>
- [16] Evans B, Walton S. Aerodynamic optimisation of a hypersonic reentry vehicle based on solution of the Boltzmann–BGK equation and evolutionary optimisation. *Applied Mathematical Modelling*. 2017;52:215-240.
- [17] Muntz E, Weaver D, Campbell D. Rarefied Gas Dynamics : Theoretical and Computational Techniques. Washington, DC: American Institute of Aeronautics and Astronautics; 1989.